

Extracting ROI-Based Contourlet Subband Energy Feature From the sMRI Image for Alzheimer's Disease Classification

Jinwang Feng¹, Shao-Wu Zhang¹, Luonan Chen¹, and Alzheimer's Disease Neuroimaging Initiative¹

Abstract—Structural magnetic resonance imaging (sMRI)-based Alzheimer's disease (AD) classification and its prodromal stage—mild cognitive impairment (MCI) classification have attracted many attentions and been widely investigated in recent years. Owing to the high dimensionality, representation of the sMRI image becomes a difficult issue in AD classification. Furthermore, regions of interest (ROI) reflected in the sMRI image are not characterized properly by spatial analysis techniques, which has been a main cause of weakening the discriminating ability of the extracted spatial feature. In this study, we propose a ROI-based contourlet subband energy (ROICSE) feature to represent the sMRI image in the frequency domain for AD classification. Specifically, a preprocessed sMRI image is first segmented into 90 ROIs by a constructed brain mask. Instead of extracting features from the 90 ROIs in the spatial domain, the contourlet transform is performed on each of these ROIs to obtain their energy subbands. And then for an ROI, a subband energy (SE) feature vector is constructed to capture its energy distribution and contour information. Afterwards, SE feature vectors of the 90 ROIs are concatenated to form a ROICSE feature of the sMRI image. Finally, support vector machine (SVM) classifier is used to classify 880 subjects from ADNI and OASIS databases. Experimental results show that the ROICSE approach outperforms six other state-of-the-art methods, demonstrating that energy and contour information of the ROI are important to capture differences between the sMRI images of AD and HC subjects. Meanwhile, brain regions related to AD can also be found using the ROICSE feature, indicating that the ROICSE feature can be a promising assistant imaging marker for the AD diagnosis via the sMRI image. Code and Sample IDs of this paper can be downloaded at <https://github.com/NWPU-903PR/ROICSE.git>.

Index Terms—Alzheimer's disease, image classification, regions of interest, contourlet transform, subband energy feature

1 INTRODUCTION

WITH the development of medical imaging techniques and equipments, structural magnetic resonance imaging (sMRI) has become one of main modalities for brain disease diagnosis in clinics [1], [2], [3]. In recent years, Alzheimer's disease (AD) is expected to be a primary cause of

dementia, which is characterized by cognitive impairment, behavior disorder, memory loss, and decline of living ability [4], [5], [6], [7], [8], [9]. In 2006, there were a reported 26.6 million AD cases worldwide, about 56 percent of which were at the early stage [10]. When the year 2050, the population of AD patients is predicted to grow by more than four-fold to 106.8 million, and one in 85 persons will be affected by this disease [11]. Therefore, it is becoming an urgent issue for clinicians to identify AD and mild cognitive impairment (MCI, the prodromal stage of AD) patients from healthy control (HC) subjects, and subsequently delay or stop its neurodegenerative progression.

To solve the problem of inaccurately identifying AD patients, a majority of researchers have put their attention on how to construct a powerful marker in line with sMRI images [12], [13], [14], [15], [16], [17], [18], [19], [20]. According to those existing works, AD classification methods can be roughly divided into three categories: voxel (or vertex)-based [21], [22], [23], [24], [25], regions of interest (ROI)-based [26], [27], [28], [29], and patch-based methods [30], [31], [32]. In the voxel-based method, features are simply extracted based on statistics or selection of voxels. Ju *et al.* proposed to use deep learning with brain network and clinical relevant text information to make early diagnosis of Alzheimer's disease [33]. However, the voxel-based features usually have much higher dimensionality and noisy, which may not be related to the disease. Thus, the dimensions of the voxel-based features need be reduced by techniques such as smoothing [34], downsampling [35] and feature selection [36] so that the classifiers are more effective and

1. Data used in preparation of this article were obtained from the Alzheimer's Disease Neuroimaging Initiative (ADNI) database (adni.loni.usc.edu). As such, the investigators within the ADNI contributed to the design and implementation of ADNI and/or provided data but did not participate in analysis or writing of this report. A complete listing of ADNI investigators can be found at: http://adni.loni.usc.edu/wp-content/uploads/how_to_apply/ADNI_Acknowledgement_List.pdf

- Jinwang Feng and Shao-Wu Zhang are with the Key Laboratory of Information Fusion Technology of Ministry of Education, School of Automation, Northwestern Polytechnical University, Xi'an 710072, China.
E-mail: jinxwangfeng11@163.com, zhangsw@nwpu.edu.cn.
- Luonan Chen is with the Key Laboratory of Information Fusion Technology of Ministry of Education, School of Automation, Northwestern Polytechnical University, Xi'an 710072, China, the Key Laboratory of Systems Biology, Shanghai Institute of Biochemistry and Cell Biology, Center for Excellence in Molecular Cell Science, Chinese Academy of Sciences, Shanghai 200031, China, the Key Laboratory of Systems Biology, Hangzhou Institute for Advanced Study, University of Chinese Academy of Sciences, Chinese Academy of Sciences, Hangzhou 310024, China, and also with the School of Life Science and Technology, ShanghaiTech University, Shanghai 201210, China.
E-mail: lnchen@sibs.ac.cn.

Manuscript received 7 Oct. 2019; revised 28 Dec. 2020; accepted 9 Jan. 2021.
Date of publication 12 Jan. 2021; date of current version 3 June 2022.
(Corresponding authors: Shao-Wu Zhang and Luonan Chen.)
Digital Object Identifier no. 10.1109/TCBB.2021.3051177

efficient. In the ROI-based method, a brain sMRI image is segmented into different tissue ROIs, and then an ROI-based feature vector or a vector of the relationships between those ROIs is used to describe the sMRI image in classifying AD patients. Ahmed *et al.* developed an automatic classification framework for AD recognition using hippocampal visual features [37]. However, spatial features used to represent an ROI do not capture direction and multiscale information; Moreover, dimensions of the ROI-based features are relatively high and still need to be further reduced. For the patch-based method, a tissue patch containing multiple ROIs is selected to extract spatial features. Li *et al.* developed a deep learning method to segment hippocampus from MRI data for predicting MCI subjects' progression to AD dementia in a time-to-event analysis setting [38]. Meanwhile, Khedher *et al.* presented a new CAD system that allows early AD diagnosis using tissue-segmented brain images [39]. It is clear that some important information related to AD is ignored by the patch-based features in describing the sMRI image.

From the perspective of image processing, we prefer to divide AD classification methods into the spatial domain-based and the transformation domain-based methods [40], [41], [42]. The former can easily describe an image by analyzing its structural patterns in the spatial domain, including voxel-based, ROI-based, patch-based, and deep learning (DL)-based features. For the DL-based method, features are automatically extracted from structural patterns of the sMRI image by different network models [6], [9], [43], [44], [45]. Liu *et al.* [44] proposed a multi-model DL framework based on convolutional neural network (CNN) for joint automatic hippocampal segmentation and AD classification with structural MRI data. Wang *et al.* [45] provided a new computer-vision based technique to detect AD in an efficient way using eight-layer CNN with leaky rectified linear unit and max pooling. For the latter, an image is first transformed by the wavelet, contourlet, or shearlet to obtain its subbands [46]. The subbands are then used to construct energy features in the frequency domain. Over the past decade, there have been few existing features extracted by the transformation domain-based method for AD classification. Nowadays, the transformation domain-based method gradually appears. For example, Zhang *et al.* utilized stationary wavelet entropy to extract the texture features of an MRI for AD classification [47], and Jha *et al.* proposed a novel computer-aided diagnosis (CAD) cascade model to discriminate patients with AD from healthy controls using the dual-tree complex wavelet transforms [48]. However the challenge of the transformation domain-based method is how to make a trade-off between the feature dimensionality and the decomposition scale, as well as how to reasonably segment subbands into different energy regions.

In order to alleviate problems of the curse of dimensionality and the segmentation to subband, and extract features with biological meanings, an ROI-based contourlet subband energy (ROICSE) feature is proposed to represent the sMRI image in the frequency domain for AD classification. Specifically, a preprocessed sMRI image is first segmented into 90 different ROIs by a constructed brain mask that is made based on the anatomical automated labeling (AAL) atlas [49]. Instead of extracting features from these ROIs in the spatial domain directly, the contourlet transform is performed on

each of the 90 ROIs to obtain their subbands, which guarantees that the segmentation to subband is avoided and features extracted from the subbands have biological meanings. Next, a subband energy (SE) feature vector is constructed to capture energy and contour information for representing the ROIs. Subsequently, SE feature vectors of the 90 different ROIs are concatenated to form the ROICSE feature for representing the sMRI image. Finally, the support vector machine (SVM) classifier is selected to categorize subjects with AD, MCI and HC based on the ROICSE feature. Experimental results show that the ROICSE approach outperforms six other state-of-the-art methods in terms of sensitivity, specificity, and accuracy and so on, demonstrating that energy and contour information of the ROI are important to capture differences between sMRI images of the AD and HC subjects. Meanwhile brain regions related to AD can also be found using the ROICSE feature, indicating that the ROICSE feature can be a promising assistant imaging marker for the AD diagnosis via the sMRI image.

Two main contributions have been made in this study. First, a new method is proposed to construct a low-dimensional representation of the sMRI image for AD classification, which can extract the frequency domain-based feature from different brain regions, guaranteeing that the extracted features have special biological meanings and can further find brain regions related to AD. Second, different from the common approaches performing the contourlet transform on images directly, the proposed ROICSE method first partitions the sMRI image into different ROIs based on the constructed brain mask in the spatial domain, and then the contourlet transform is performed on those ROIs to obtain subbands in the frequency domain. This new strategy can integrate advantages of both the spatial and the frequency domain-based techniques, which make sure that the ROI can be properly represented using features extracted from the contourlet subbands.

The rest of this study is organized as follows: In Section 2, materials and methods are introduced in detail; Metrics and experimental results are included in Section 3; Discussion is made in Section 4; Finally, a brief conclusion to this study is given in Section 5.

2 MATERIALS AND METHODS

In this section, materials and their preprocessing are introduced first, followed by the framework of extracting the ROICSE feature.

2.1 Materials

Data used in the preparation of this article were obtained from the Alzheimer's Disease Neuroimaging Initiative (ADNI) database (adni.loni.usc.edu). The ADNI was launched in 2003 as a public-private partnership, led by Principal Investigator Michael W. Weiner, MD. The primary goal of ADNI has been to test whether serial magnetic resonance imaging (MRI), positron emission tomography (PET), other biological markers, and clinical and neuropsychological assessment can be combined to measure the progression of mild cognitive impairment (MCI) and early Alzheimer's disease (AD).

Nowadays, the sMRI image has been one of the widely used modalities in clinically distinguishing AD and MCI

TABLE 1
Demographic Information of the 880 Selected Subjects

Database	Type	Gender (F/M)	No.	Age (Mn±D)	MMSE (Mn±D)
ADNI	AD	78/122	200	76.85±7.01	22.15±3.17
	MCIC	67/53	120	78.65±9.73	26.38±3.76
	MCInc	71/89	160	73.59±7.68	26.21±2.67
	MCI	138/142	280	75.76±8.96	26.28±3.17
	HC	84/116	200	76.21±4.97	29.09±1.15
OASIS	AD	56/44	100	76.07±7.63	21.18±4.30
	HC	63/37	100	60.28±3.79	29.42±0.77

from healthy control (HC) subjects. At the clinical diagnosis stage, patients with MCI can also be divided into subjects who will convert into AD after 18 months and subjects who will remain stable after 18 months. In this study, these two subcategories are denoted as MCIC and MCInc, respectively. To evaluate classification performance of the ROICSE feature, 880 sMRI images, including 300 AD, 120 MCIC, 160 MCInc, and 300 HC, are selected from ADNI and OASIS databases. More detail demographic information about these selected sMRI images are summarized in Table 1. MMSE, F, M, Mn, and D in Table 1 are separately abbreviations of Mini Mental State Examination, Female, Male, Mean, and Deviation.

For those selected sMRI images, a four-step preprocessing, including motion correction, registration and skull strap, segmentation, and smoothing, is performed using statistic parametric mapping (SPM8) [50] and voxel-based mapping (VBM8) [51] to remove unrelated tissues and ensures that a certain brain region of different subjects is at the same position. After preprocessing steps, the sMRI image is segmented into $121 \times 145 \times 121$ gray matter (GM), cerebrospinal fluid (CSF), and white matter (WM) images, and the voxel volume is $1.5 \times 1.5 \times 1.5 \text{ mm}^3$.

At the experimental stage, the GM image that is mostly related to AD is selected to extract the ROICSE feature, and five data sets are constructed to perform experiments, which are described as follows:

- 1) AD/HC: containing 200 AD and 200 HC subjects from the ADNI database;
- 2) AD/MCI: containing 200 AD and 280 MCI subjects from the ADNI database;
- 3) MCI/HC: containing 280 MCI and 200 HC subjects from the ADNI database;
- 4) MCIC/MCInc: containing 120 MCIC and 160 MCInc subjects from the ADNI database.
- 5) OASIS: containing 100 AD and 100 HC subjects from the OASIS database.

Obviously, MCIC/MCInc is a challenging data set whose subjects are MCI patients.

2.2 Method of Extracting the ROICSE Feature

For those gray matter (GM) images, we use a subject set $\{GM_t^i\}$ to represent them, where $i \in [1, 880]$ is the i th subject, and $t \in [1, 121]$ is the t th scan of the i th subject. Before segmenting the GM image into different brain regions of

interest (ROI), a mask need be made based on the anatomical automated labeling (AAL) atlas.

The single ROI mask set of 90 brain regions is first made using the AAL atlas. This set is denoted as $\{AAL_{p,t}\}$, $p = 1, 2, \dots, 90$, $t = 1, 2, \dots, 91$, where p is the p th single ROI mask, and t is the t th scan contained in the p th single ROI mask. While the size and voxel volume of the single ROI mask are $91 \times 109 \times 91$ and $2 \times 2 \times 2 \text{ mm}^3$, respectively, which are inconsistent with the size and volume of the pre-processed GM images. So co-registration must be done between the single ROI mask and the GM image by SPM8. After co-registration, the size and voxel volume of the single ROI mask become $121 \times 145 \times 121$ and $1.5 \times 1.5 \times 1.5 \text{ mm}^3$, respectively. Therefore, the number of scans contained in the GM image and the single ROI mask is the same, and thus the same subscript t is used in sets $\{GM_t^i\}$ and $\{AAL_{p,t}\}$. Then a mask containing 90 brain ROIs and denoted as $Mask_t$ can be constructed, which is formulated by

$$Mask_t(x, y) = p, \text{ if } AAL_{p,t}(x, y) = 1, p = 1, \dots, 90, \quad (1)$$

where (x, y) is a position in the p th single ROI mask. Obviously, $x = 1, 2, \dots, 121$ and $y = 1, 2, \dots, 145$.

Based on the constructed brain mask $Mask_t$, we can segment the GM images in $\{GM_t^i\}$, into different brain ROIs. For a GM image of the i th subject GM_t^i , its p th brain ROI can be represented by

$$ROI_p^i(x, y) = \begin{cases} GM_t^i(x, y), & \text{if } Mask_t(x, y) = p \\ 0, & \text{Otherwise} \end{cases} \quad (2)$$

where (x, y) is a position in the t th scan contained in $Mask_t$ and GM_t^i , $t = 1, 2, \dots, 121$, and $p = 1, 2, \dots, 90$. For simplicity, we use a set denoted as $\{ROI_p^i\}$ to represent the ROIs of all GM images, where i is the i th subject, and p is the p th brain ROI of the i th subject.

Multiscale analysis is an important transform technique in the field of image processing [5], [13]. Contourlet and curvelet are two widely used transform tools, which can conquer linear singularity and capture intrinsic geometrical structures of images perfectly [52], [62], [63]. Compared with the contourlet, though the curvelet can transform an image into different scales and directions, more redundant information is generated at the detail scales [62]. In contrast, as shown in Fig. 1, the contourlet transform is a down-sampling process, which can avoid information redundancy to some extent. Meanwhile, except the scale and direction parameters, the curvelet has a third parameter-location-needed to be set. Furthermore, it is obvious that Alzheimer is a disease with lesions to multiple brain regions, contours of the lesion regions are different from those of the healthy control, thus the contour information of different brain ROIs can be used as one of the markers for identifying the AD patient. According to the above facts, the contourlet transform is more suitable to be selected by the ROICSE method.

Given the p th brain ROI of the i th GM image ROI_p^i , we use the contourlet with a S -decomposition-level directional filter bank at each of the L scales to transform the ROI_p^i , that is, the number of directional subbands at each scale is 2^S . After the contourlet transform on ROI_p^i , we can obtain 2^S directional subbands at each of the L scales, hence there are $2^S \times L$ directional subbands and a low-frequency subband

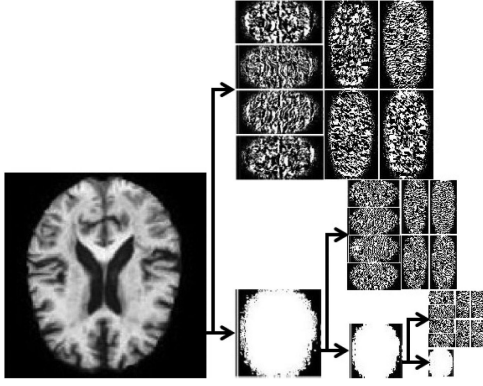


Fig. 1. The contourlet transform with transform scale $L=3$ and decomposition level $S=3$.

in total. For brevity and simplicity, a set, denoted as $\{S_{(p,j)}^i\}$, is used to represent subbands of all brain ROIs of the GM images in $\{GM_t^i\}$, where $j \in [1, 2^S \times L + 1]$ is the j th subband of the p th brain ROI of the i th GM image.

For the subband set $\{S_{(p,j)}^i\}$, it is clear that the number of subbands is determined by L and S whose optimal values will be estimated by experiments in this study. For the $2^S \times L + 1$ subbands of each brain ROI, the low-frequency subband is arranged at the first position in the subband set, and the remaining $2^S \times L$ positions of the subband set are used to arrange the directional subbands. For example, $S_{(3,1)}^2$ represents the low-frequency subband of the third brain ROI of the second GM image in $\{GM_t^i\}$.

Given a low-frequency subband and $2^S \times L$ directional subbands of the p th brain ROI of the i th GM image, we can obtain a low-frequency subband energy feature $e_{(p,0)}^i$, which is represented by

$$e_{(p,0)}^i = \frac{\sum_{x=1}^{M0} \sum_{y=1}^{N0} |S_{(p,1)}^i(x, y)|}{M0 \times N0}, \quad (3)$$

where $M0$ and $N0$ are the sizes of the low-frequency subband, and $S_{(p,1)}^i(x, y)$ is a coefficient in the low-frequency subband, and the directional subband energy feature $e_{(p,1)}^i$ is represented by

$$e_{(p,1)}^i = \frac{\sum_{j=2}^{2^S \times L + 1} \sum_{x=1}^{M1} \sum_{y=1}^{N1} |S_{(p,j)}^i(x, y)|}{2^S \times L \times M1 \times N1}, \quad (4)$$

where $M1$ and $N1$ are the sizes of the directional subbands, and $S_{(p,j)}^i(x, y)$ is a coefficient in those directional subbands.

According to Equations (3) and (4), the p th brain ROI of the i th GM image can be represented by a subband energy (SE) feature vector denoted as

$$SE_p^i = [e_{(p,0)}^i, e_{(p,1)}^i]. \quad (5)$$

By concatenating the SE feature vectors SE_p^i , where $p = 1, 2, \dots, 90$, we can obtain the final ROI-based contourlet subband energy (ROICSE) feature of the i th GM image, which is represented by

$$ROICSE^i = [SE_1^i, SE_2^i, \dots, SE_{90}^i]. \quad (6)$$

For all sMRI images selected from the ADNI and OASIS databases in this study, a feature set, denoted as $\{ROICSE^i\}$,

where $i = 1, 2, \dots, 880$, is used to describe them. Obviously the dimension of the ROICSE feature is $90 \times 2 = 180$, which is reduced to a large extent compared with the dimension of the GM image. In the subsequent section, the ROICSE features are used as imaging markers of the sMRI image for AD classification and its association analysis.

2.3 Support Vector Machine Classifier

AD classification and association analysis are realized by the ROICSE feature using support vector machine (SVM) classifier. In this study, the SVM classifier is provided by MATLAB software, and we select the radial basis function (RBF) as the kernel of the SVM classifier, which is formulated as

$$k(x1, x2) = \exp\left(-\frac{\|x1 - x2\|^2}{2\sigma^2}\right). \quad (7)$$

It is obvious that for the SVM classifier with the RBF kernel, two important parameters, the window width of the RBF kernel σ and the penalty coefficient of the SVM classifier C , need to be estimated based on experiments. σ is used to control the number of support vectors: with an increase in σ , the number of support vectors decreases, and vice versa. Meanwhile, C is used to control the penalty degree to error, with the increase of C , it easily causes over-fitting, and vice versa. Therefore, parameters σ and C , need to be estimated based on experiments carefully.

2.4 Metrics

In order to evaluate the classification performance of the ROICSE approach, we will perform ten experiments with ten-fold cross validation on those data sets. For the ten-fold cross validation experiment, subjects contained in a data set are randomly divided into ten subsets, one is used for testing, and the rest is used for training the SVM classifier. The mean classification accuracy (ACC), sensitivity (Se), specificity (Sp), precision-recall and receiver operating characteristic (ROC) curves, and Matthews correlation coefficient (MCC) of the ten experiments on each of those data sets are used as the final result, which are formulated as follows:

$$ACC = \frac{1}{10} \sum_{i=1}^{10} \frac{TP_i + TN_i}{TP_i + FP_i + TN_i + FN_i}, \quad (8)$$

$$Se = \frac{1}{10} \sum_{i=1}^{10} \frac{TP_i}{TP_i + FN_i}, \quad (9)$$

$$Sp = \frac{1}{10} \sum_{i=1}^{10} \frac{TN_i}{FP_i + TN_i}, \quad (10)$$

$$MCC = \frac{1}{10} \sum_{i=1}^{10} \frac{TP_i \times TN_i - FP_i \times FN_i}{\sqrt{TPN_i}}, \quad (11)$$

where TP_i is the number of correctly classified positive subjects, FP_i is the number of incorrectly classified negative subjects, TN_i is the number of correctly classified negative subjects, FN_i is the number of incorrectly classified positive subjects, $TPN_i = (TP_i + FP_i)(TP_i + FN_i)(TN_i + FP_i)(TN_i + FN_i)$, and the subscript i is the i th experiment on a data set. Meanwhile, precision predictive value (PPV), F1 score (F1),

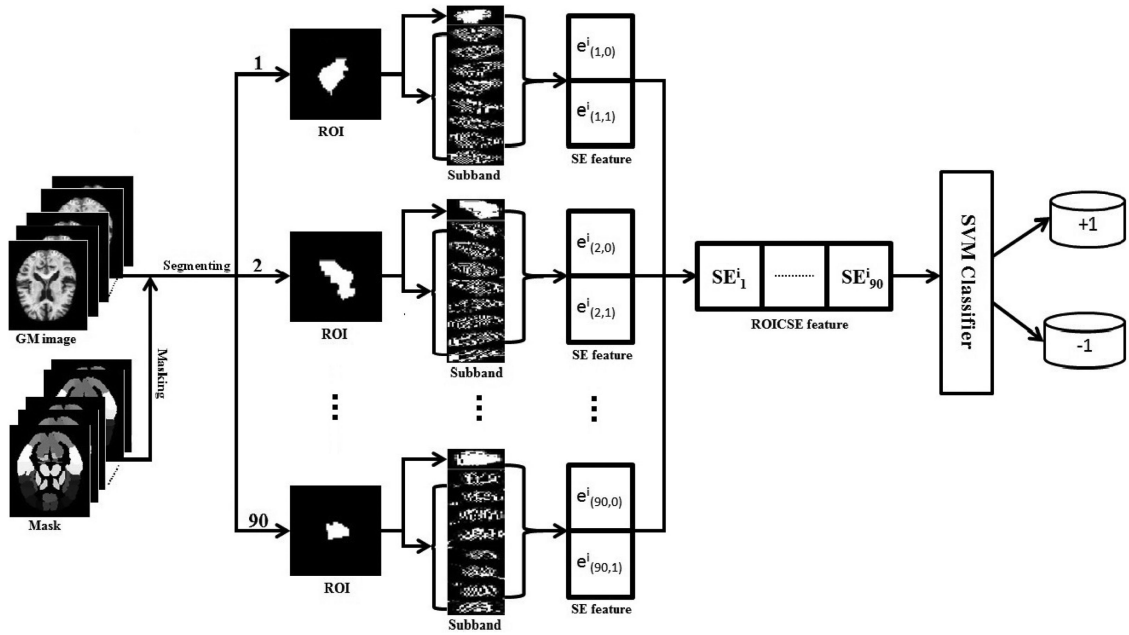


Fig. 2. The framework of extracting the ROICSE feature from the gray matter (GM) image for AD classification.

false positive rate (FPR) are also listed in Table S1 to S5, which can be found in the supplementary materials, which can be found on the Computer Society Digital Library at <http://doi.ieeecomputersociety.org/10.1109/TCBB.2021.3051177>.

In summary, for a given sMRI image, after preprocessing, we can directly obtain the GM image. Then the GM image is segmented into 90 different brain ROIs by a constructed brain mask. The contourlet transform is performed on each of the 90 ROIs to obtain their subbands, and then a SE feature vector is constructed to describe each of these ROIs. Subsequently, the SE feature vectors of the 90 ROIs are concatenated to form the ROICSE feature for being a marker of the sMRI image. Finally, the ROICSE features are used as input for the SVM classifier to classify subjects with AD, MCI, and HC. For the sake of visualization, Fig. 2 shows the completed framework of the ROICSE approach for AD classification.

3 EXPERIMENTS

In this section, we will conduct multiple experiments on AD/HC, AD/MCI, MCI/HC, MCIC/MCInc, and OASIS data sets using the ROICSE feature. Parameter selection for the ROICSE-based approach is first introduced, followed by comparison experiments on the ADNI and OASIS databases.

3.1 Parameter Selection

In the proposed approach, four parameters, the contourlet transform scale L , the decomposition level of the directional filter bands S , the window width of the RBF kernel σ , and the penalty coefficient of the SVM classifier C , are estimated by experiments on the ADNI database.

To estimate parameters of the contourlet transform L and S , we set $C = 1$ and $\sigma = 1$ when experiments are conducted on AD/HC, AD/MCI, MCI/HC, and MCIC/MCInc data sets. ACC's of experiments with different L and S values on the four data sets are shown in Fig. 3. It is clear from Figs. 3a and 3b that with the increase of L , ACC's of experiments on

the four data sets decrease rapidly, and with the increase of S , ACC's are increasing at first, and then decreasing after $S > 3$. Obviously, the ROICSE approach can get the best results overall when $L = 1$ and $S = 3$. Additionally, it can be also seen from Fig. 1 that with the increase of L , contours of different brain regions are destroyed but more detail information is contained in the subbands. Considering that Alzheimer's is a disease along with atrophies of multiple brain regions and the ROICSE feature is constructed with the contour and energy distribution information of different ROIs, therefore, we set $L = 1$ and $S = 3$ as the optimal estimation values of the contourlet transform.

To obtain the optimal estimation of the window width of the RBF kernel σ , we set the penalty coefficient of the SVM classifier $C = 1$, and use $L = 1$ and $S = 3$ in estimation experiments of the window width of the RBF kernel σ . ACC's of experiments with different window widths of the RBF kernel σ are given in Fig. 4. As is shown in Fig. 4, ACC's on the four data sets AD/HC, AD/MCI, MCI/HC, and MCIC/MCInc increase rapidly when $\sigma \leq 0.8$, ACC's increase slowly when $0.8 < \sigma < 1.0$, however ACC's on the four data sets decrease quickly when $\sigma \geq 1.0$. With the fact of Fig. 4 shown, we set $\sigma = 0.9$ (i.e., the mean value of $\sigma = 0.8$ and $\sigma = 1.0$) as the optimal estimation of the window width of the RBF kernel.

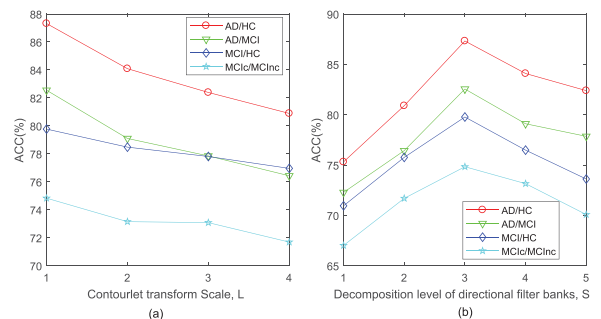


Fig. 3. ACC's of experiments with different L and S values on the ADNI database with $C = 1$ and $\sigma = 1$.

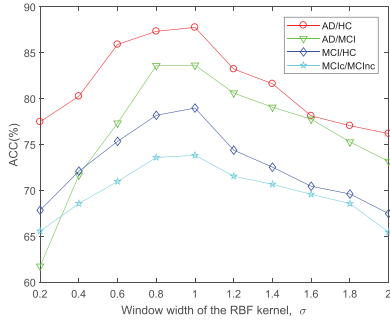


Fig. 4. ACC's of experiments with different window widths of the RBF kernel σ on the ADNI database when the penalty coefficient of the SVM classifier $C = 1$, $L = 1$, and $S = 3$.

The penalty coefficient of the SVM classifier C is estimated on AD/HC, AD/MCI, MCI/HC, and MCIc/MCIinc data sets when $L = 1$, $S = 3$, and $\sigma = 0.9$. ACC's of experiments with different penalty coefficients of the SVM classifier C on the four data sets are shown in Fig. 5. It can be clearly seen from Fig. 5 that ACC's on the four data sets increase dramatically when $C < 15$, and ACC's on the four data sets gradually become stable after $C \geq 15$. Therefore we set $C = 15$ as the optimal estimation value of the penalty coefficient of the SVM classifier based on the fact of Fig. 5 shown.

Finally, ACCs of the ROICSE approach using SVM with RBF on the ADNI and OASIS databases are shown in Table 2 when $L = 1$, $S = 3$, $\sigma = 0.9$, and $C = 15$. Meanwhile, ACCs of the ROICSE approach using SVM with Polynomial and Linear kernels are also listed in Table 2. It is obvious from Table 2 that ACCs of the ROICSE approach using SVM with RBF are better than those of SVM with Polynomial and Linear on the two databases. That is why the SVM classifier with RBF is selected in the ROICSE approach.

3.2 Comparisons

In the following, we will compare the ROICSE approach with six other state-of-the-art methods on ADNI and OASIS databases under the same settings when parameters of the ROICSE approach, $L = 1$, $S = 3$, $\sigma = 0.9$, and $C = 15$, followed by comparisons with published results of machine learning-based algorithms.

3.2.1 Comparisons on the ADNI Database

On the AD/HC data set, we evaluate the classification performance of the ROICSE approach in identifying AD patients from HC subjects. ACC's, Se's, Sp's, and MCC's of

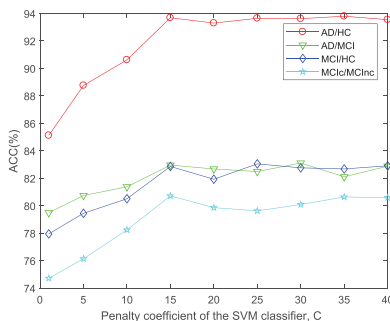


Fig. 5. ACC's of experiments with different penalty coefficients of the SVM classifier C on the ADNI database when $L = 1$, $S = 3$, and $\sigma = 0.9$.

TABLE 2
ACCs of the ROICSE Approach Using SVM With RBF, Polynomial, and Linear Kernels on ADNI and OASIS Databases When $L = 1$, $S = 3$, $\sigma = 0.9$, and $C = 15$

Databases	Data sets	RBF	Polynomial	Linear
ADNI	AD/HC	93.57	91.07	89.43
	AD/MCI	82.73	80.59	78.36
	MCI/HC	83.13	81.00	79.02
	MCIc/MCIinc	77.29	75.12	73.21
OASIS	AD/HC	82.55	80.17	75.69

the six comparison methods and the ROICSE approach are listed in Table 3. According to ACC's shown in Table 3, ACC of the ROICSE approach is marginally higher than those of the six state-of-the-art methods, has reached to 93.57 percent, and is 0.65 percent higher than that of the best comparison method. Additionally, Se, Sp, and MCC of the ROICSE approach consistently outperform those of the six state-of-the-art methods and are 95.83 percent, 91.87 percent, and 0.85, respectively. Experimental results on the AD/HC data set demonstrate that differences between sMRI images of the AD and HC subjects can be captured by contourlet subbands, and also testify the rationality of doing the contourlet transform on brain ROIs.

To perform an extensive comparison with the six state-of-the-art methods, experiments on the AD/MCI data set are conducted, and ACC's, Se's, Sp's, and MCC's of the six state-of-the-art methods and the ROICSE approach are given in Table 4. It is clear from Table 4 that ACC of the ROICSE approach is 82.73 percent, which is a little higher than the best comparison method's 82.59 percent. Moreover, Se, Sp, and MCC of the ROICSE approach consistently outperform those of the six state-of-the-art methods, which are 84.65 percent, 80.80 percent, and 0.66, respectively. Experimental results on the AD/MCI data set also indicate that the transformation domain-based tool can be used to analyze the MRI image, and contour and multiscale information contained in the subband are captured by the ROICSE feature.

To make a further evaluation, experiments are done on the MCI/HC data set. ACC's, Se's, Sp's, and MCC's of the six state-of-the-art methods and the ROICSE approach are listed in Table 5. It can be observed from Table 5 that ACC of the ROICSE approach is 83.13 percent, this result is still marginally higher than the best comparison method's 83.09 percent. However, Se, Sp, and MCC of the ROICSE approach are 87.79 percent, 76.60 percent, and 0.65, respectively, which are

TABLE 3
Results of the Six Comparison Methods and the ROICSE Approach on AD/HC Data Set

Method	ACC(%)	Se(%)	Sp(%)	MCC
HippoV [37]	85.70	77.61	91.28	0.71
Hippo [38]	87.51	87.60	87.42	0.76
TSB [39]	89.96	92.35	86.94	0.79
AUTO [33]	92.92	94.00	89.85	0.85
DTCW [48]	90.16	90.22	90.15	0.80
SWE [47]	92.70	93.67	91.77	0.85
ROICSE	93.57	95.83	91.87	0.85

TABLE 4
Results of the Six Comparison Methods and the ROICSE
Approach on AD/MCI Data Set

Method	ACC(%)	Se(%)	Sp(%)	MCC
HippoV [37]	71.51	75.94	71.23	0.43
Hippo [38]	79.35	79.44	79.26	0.60
TSB [39]	81.53	83.75	80.07	0.63
AUTO [33]	82.59	84.26	80.11	0.65
DTCW [48]	78.48	75.35	79.98	0.57
SWE [47]	80.49	76.21	80.65	0.61
ROICSE	82.73	84.65	80.80	0.66

TABLE 5
Results of the Six Comparison Methods and the ROICSE
Approach on MCI/HC Data Set

Method	ACC(%)	Se(%)	Sp(%)	MCC
HippoV [37]	76.29	72.30	81.53	0.49
Hippo [38]	77.25	95.79	53.23	0.53
TSB [39]	82.41	84.12	80.48	0.63
AUTO [33]	83.09	83.46	82.31	0.65
DTCW [48]	81.94	75.79	84.18	0.61
SWE [47]	80.67	76.79	86.98	0.57
ROICSE	83.13	87.79	76.60	0.65

not more than 95.79 percent, 86.98 percent, and 0.65 of the best comparison methods. Based on Tables 4 and 5, we can find that the ROICSE approach marginally outperforms the comparison methods. The reason for this is that subjects with MCI are anisotropic in their sMRI images, and MCInc subjects have more AD-like pathological patterns and in contrast, MCInc subjects have more HC-like pathological patterns.

For MCInc/MCInc, it is a more challenging data set for the ROICSE approach in classifying MCInc from MCInc patients, due to the fact that only tiny differences can be found between their sMRI images. We still give ACC's, Se's, Sp's, and MCC's of the six state-of-the-art methods and the ROICSE approach, which are shown in Table 6. It is obvious from Table 6 that ACC of the ROICSE approach is 77.29 percent, which is 4.43 percent higher than the best comparison method's 72.86 percent. In addition, Se and MCC of the ROICSE approach consistently outperforms those of the six state-of-the-art methods, and reaches 80.36 percent and 0.61. Conversely, Sp of the ROICSE approach is lower than that of the best comparison method. According to experimental results listed in Table 6, we can prove that patients who will convert to AD are different from those who will remain stable in their subband energy distributions. This is why the ROICSE approach obviously outperforms the six state-of-the-art methods on the MCInc/MCInc data set.

It is obvious from Tables 3, 4, 5, and 6 that the ROICSE feature can be relatively accuracy to describe the sMRI images of subjects with AD, MCI and HC. There are three reasons: First, a constructed mask is used to segment the GM image into different ROIs; Second, the contourlet transform is performed on the ROIs to obtain subbands of the ROI; Third, the ROICSE feature is constructed with contour and energy distribution information of the ROI.

Meanwhile, in order to verify accurate representation to the sMRI image by the ROICSE feature, ROC curves of the

TABLE 6
Results of the Six Comparison Methods and the ROICSE
Approach on MCInc/MCInc Data Set

Method	ACC(%)	Se(%)	Sp(%)	MCC
HippoV [37]	68.72	67.38	70.69	0.37
Hippo [38]	69.38	69.47	69.29	0.42
TSB [39]	70.11	68.61	74.16	0.41
AUTO [33]	72.32	72.21	73.06	0.46
DTCW [48]	69.21	70.74	67.45	0.39
SWE [47]	72.86	69.55	75.49	0.49
ROICSE	77.29	80.36	74.20	0.61

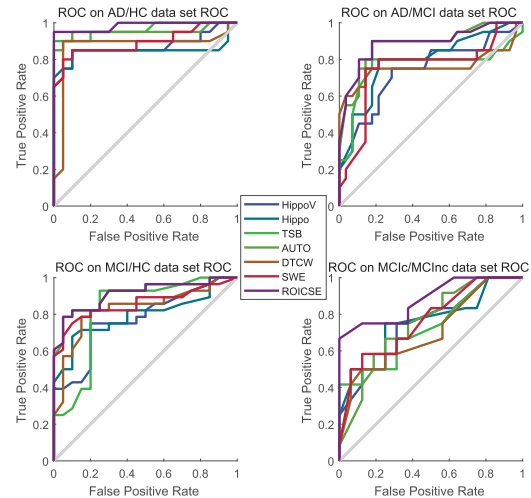


Fig. 6. ROC curves of comparison methods and the ROICSE approach on AD/HC, AD/MCI, MCI/HC, and MCInc/MCInc data sets.

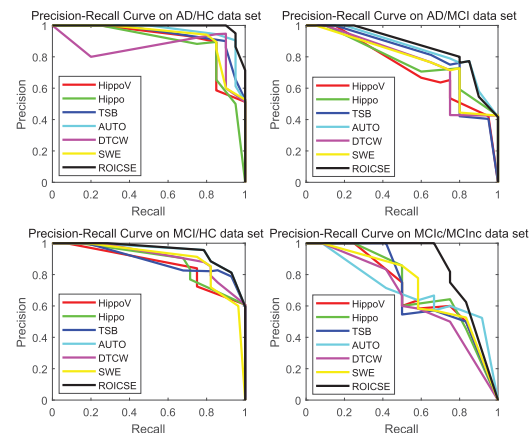


Fig. 7. Precision-recall curves of comparison methods and ROICSE on AD/HC, AD/MCI, MCI/HC, and MCInc/MCInc data sets.

comparison methods and the ROICSE approach are shown in Fig. 6. It can be seen from Fig. 6 that ROC curves of the ROICSE approach consistently outperform those of the six comparison methods on AD/HC, AD/MCI, MCI/HC, and MCInc/MCInc data sets, which are closer to the upper left of the axes. Additionally, precision-recall curves of the ROICSE approach on AD/HC, AD/MCI, MCI/HC, and MCInc/MCInc data sets are also given to evaluate the performance of the ROICSE feature extracting model. As Fig. 7 shown, precision-recall curves of the ROICSE approach also consistently outperform those of the six comparison methods, which

TABLE 7
Comparisons of Our Results With Published Results of Machine Learning-Based Methods on AD/HC and MCI/HC Data Sets

Method	Subjects	AD/HC (%)			MCI/HC (%)		
		ACC	Se	Sp	ACC	Se	Sp
DMTFS [60]	51AD+99MCI+52NC	87.30	88.40	86.20	68.20	76.90	51.10
LBFE [61]	51AD+99MCI+52NC	83.10	80.50	85.10	73.60	75.30	69.70
MKMFA [7]	192AD+397MCI+229NC	88.60	85.70	90.40	71.90	79.00	60.70
DLASAE [9]	65AD+169MCI+77NC	87.80	88.60	87.20	76.92	74.29	78.13
VGGNet [6]	97AD+233MCI+119NC	84.70	77.30	90.80	70.90	81.90	65.20
DenseNet [44]	97AD+233MCI+119NC	88.90	86.60	90.80	76.20	79.50	69.80
ROICSE	200AD+280MCI+200NC	93.57	95.83	91.87	83.13	87.79	76.60

are closer to the upper right of the axes. Experimental results on the ADNI database prove that the ROICSE approach outperform the six comparison methods in terms of classification and ROC and precision-recall curves.

In recent years, machine learning-based systems, especially the deep learning (DL)-based ones, have achieved significant performance for AD classification. Hence, we also consider quantitatively comparing results of the ROICSE approach with some recent learning-based methods published on AD/HC and MCI/HC data sets, including the conventional learning-based methods(DMTFS [60], LBFE [61], MKMFA [7]) and the DL-based methods(DLASAE [9], VGGNet [6], DenseNet [44]). Results and experimental settings obtained from their original papers are directly listed in Table 7 because the experiments are performed under different conditions. It is obvious from Table 7 that the ROICSE approach can more accurately identify AD patients from HC individuals than those DL-based methods. One reason is that for the DL-based methods, the input layer contains more than ten thousand nodes because of the high dimensionality of the sMRI image, causing a huge number of parameters to DL framework, but samples can be used to train network architecture are small. So, the DL-based features cannot accurately represent the sMRI image. Furthermore, the sMRI image contains a lot of redundant information such as the black background; therefore the useful information may not be dominant in the extracted feature, which is another reason that makes the DL-based feature with relatively low discrimination.

3.2.2 Comparisons on the OASIS Database

For validating generalization ability of the ROICSE approach, experiments on OASIS data set are conducted to compare the ROICSE approach with the six state-of-the-art methods when parameters of the ROICSE approach, $L = 1$,

$S = 3$, $\sigma = 0.9$, and $C = 15$. ACC's, Se's, Sp's, and MCC's are listed in Table 8. It is can be seen from Table 8 that ACC, Se, Sp, and MCC of the ROICSE approach consistently outperform those of the six comparison methods, which are 82.55 percent, 84.80 percent, 80.30 percent, and 0.64, respectively. Experimental results on the OASIS database further demonstrate that energy distribution and contour information of the ROI can be used as features for representing the sMRI image, and the ROICSE feature can be regarded as a promising imaging marker for identifying AD patients.

Comprehensive experimental results demonstrate that the ROICSE approach outperforms the six state-of-the-art methods and may be an useful assistance in the clinical AD diagnosis via sMRI images. Furthermore, results of the ROICSE approach indicates that the transformation domain-based tool can be introduced to analyze sMRI images for AD classification. Finally we also give the mean running time (MRT, in seconds) of the ROICSE method on MCIC/MCINC data set in identifying 160 subjects. The program runs on Matlab R2017a and computer with Intel(R) Core(TM) i7-4700 3.40 GHz CPU 64bit system. MRT of extracting the ROICSE feature from the GM image is 1.4431s, MRT of classifying a subject using the ROICSE feature is 0.0028s, and MRT of the proposed method categorises a subject is 1.4459s. Obviously, the ROICSE feature extraction is time-consuming in the ROICSE method, but it can be accepted to identify a subject using the ROICSE feature within two seconds.

4 DISCUSSION

AD has been a common cause of dementia in recent years, mainly destroying brain neurons of patients [53], [54], [55]. In this section, we will find those brain ROIs related to AD by multiple experiments. In the ROICSE approach, different brain ROIs are represented by contourlet subband energy features, which are used to construct the ROICSE feature, and therefore we can tell which brain ROI plays an important role in AD classification by exclusion. Due to the fact that the human brain is symmetric and a tissue region is represented by two brain ROIs located in different hemisphere [56], [57], so a brain can be essentially represented by 45 tissue regions. Names of the 45 ROIs are listed in Table S6 put in the supplementary materials, available online. In the following, experiments to find ROI related to AD from the 45 brain ROIs are conducted on AD/HC, AD/MCI, MCI/HC, and MCIC/MCINC data sets, and the ROICSE feature is used as a reference, which means that a brain ROI makes the positive contribution to ACC in AD classification when ACC of the ROICSE feature with the ROI removed is lower than the reference, and vice versa.

TABLE 8
Results of the Six Comparison Methods and the ROICSE Approach With $L = 1$, $S = 3$, $\sigma = 0.9$, and $C = 15$ on OASIS Data Set

Method	ACC(%)	Se(%)	Sp(%)	MCC
HippoV [37]	76.40	78.27	74.53	0.37
Hippo [38]	78.60	80.40	76.80	0.38
TSB [39]	79.55	81.70	77.40	0.42
AUTO [33]	81.27	83.04	79.50	0.62
DTCW [48]	80.74	82.99	78.49	0.60
SWE [47]	81.15	83.15	79.15	0.62
ROICSE	82.55	84.80	80.30	0.64

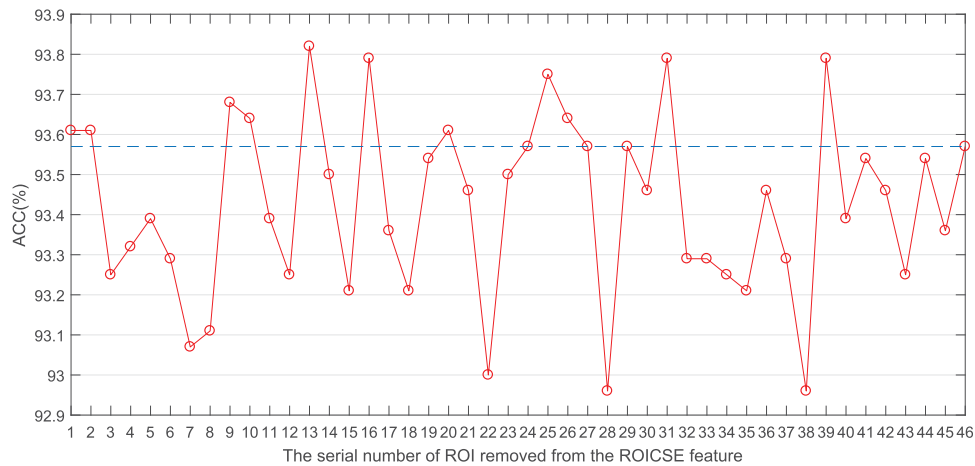


Fig. 8. ACC's of the ROICSE feature with one ROI removed and the reference on AD/Hc data set. The serial numbers from 1 to 45 in x-axis are the removed brain ROIs, and the serial number 46 in x-axis represents the reference.

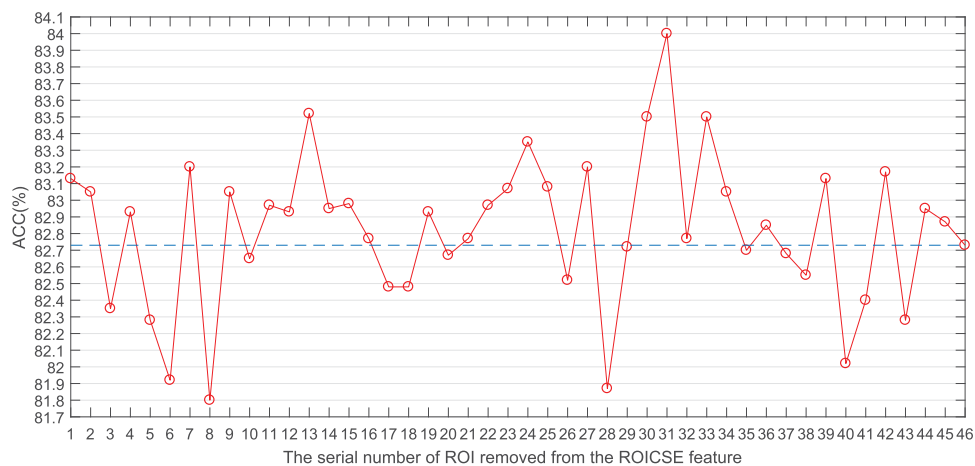


Fig. 9. ACC's of the ROICSE feature with one ROI removed and the reference on AD/MCI data set. The serial numbers from 1 to 45 in x-axis are the removed brain ROIs, and the serial number 46 in x-axis represents the reference.

To research the problem of which brain ROIs play a dominant role in classifying AD patients from HC subjects, experiments with one ROI removed from the ROICSE feature are performed on the AD/Hc data set. ACC's of the ROICSE feature with one ROI removed and the reference on the AD/Hc data set are shown in Fig. 8. It is clear from Fig. 8 that not all the brain ROIs are important in AD and HC classification. Most of the 45 brain ROIs make positive contributions to improving the ACC, some of the 45 brain ROIs make negative contributions to the ACC, three of the 45 brain ROIs do no-contributions to ACC, and ACC of the ROICSE feature-based approach changes from 92.97 to 93.83 percent on the AD/Hc data set. The first ten positive brain ROIs includes 7 (inferior frontal gyrus triangular), 8 (inferior frontal gyrus orbital), 12 (superior frontal medial), 15 (Insula), 22 (calcarine fissure surrounding cortex), 28 (fusiform gyrus), 34 (precuneus), 35 (paracentral lobule), 38 (lenticular nucleus pallidum), and 43 (middle temporal gyrus). Brain ROIs such as 13 (superior frontal gyrus medial orbital), 16 (anterior cingulate paracingulate gyri), 25 (superior occipital gyrus), 31 (inferior parietal gyri), and 39 (thalamus) all make negative contributions to ACC in AD and HC classification. In addition, three brain ROIs do no-contributions to the ACC, which are 24 (lingual gyrus), 27

(inferior occipital gyrus), and 29 (postcentral gyrus). Those results show that multiple brain regions have been affected by this disease, and indicate that feature selection is needed in extracting energy information from the brain ROIs.

For the AD/MCI data set, experiments with one brain ROI removed from the ROICSE feature are also performed to research the problem of which brain ROI plays a dominant role in classifying AD from MCI patients. ACC's of the ROICSE feature with one ROI removed and the reference are given in Fig. 9. We can tell from Fig. 9 that not all brain ROIs are important in AD and MCI classification, most of the 45 brain ROIs make negative contributions to ACC, the number of brain ROIs doing positive contributions to ACC is less than half of the total, and the ACC interval of the ROICSE approach is 81.80–84.00 percent on the AD/MCI data set. Specifically, 3 (superior frontal gyrus orbital), 5 (middle frontal gyrus orbital), 6 (inferior frontal gyrus opercular), 8 (inferior frontal gyrus orbital), 17 (median cingulate paracingulate gyri), 18 (posterior cingulate gyrus), 28 (fusiform gyrus), 40 (heschl gyrus), 41 (superior temporal gyrus), and 43 (middle temporal gyrus) are the first ten brain ROIs which make more positive contributions to ACC. The no-contribution brain ROI is null, which means that the 45 brain ROIs are divided into two classes. According to the number of brain ROIs making negative

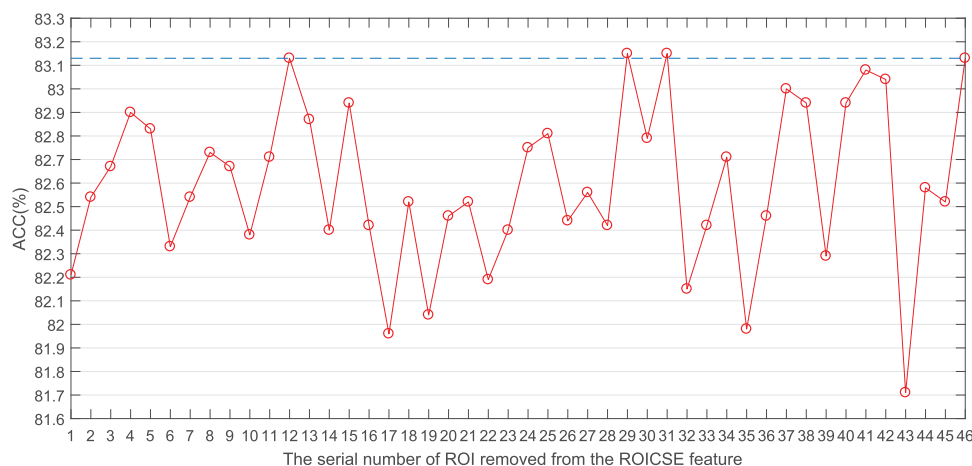


Fig. 10. ACC's of the ROICSE feature with one ROI removed and the reference on MCI/HC data set. The serial numbers from 1 to 45 in x-axis are the removed brain ROIs, and the serial number 46 in x-axis represents the reference.

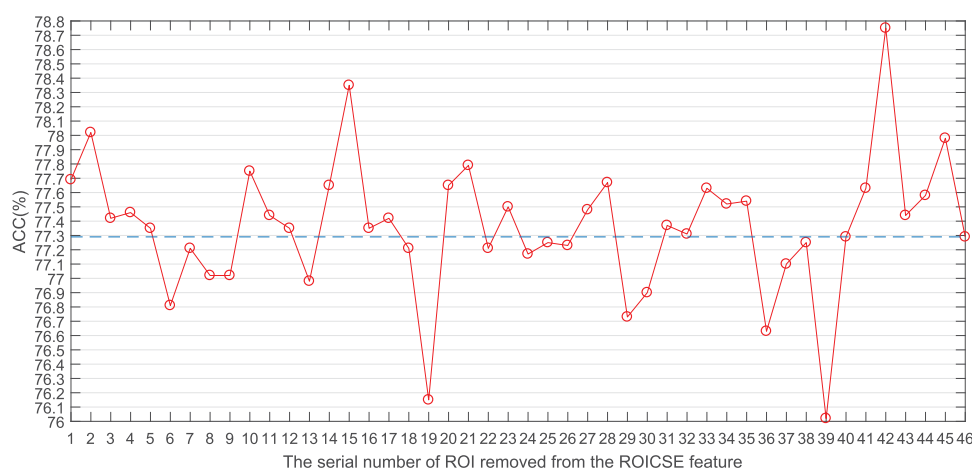


Fig. 11. ACC's of the ROICSE feature with one ROI removed and the reference on MCIC/MCInc data set. The serial numbers from 1 to 45 in x-axis are the removed brain ROIs, and the serial number 46 in x-axis represents the reference.

contributions, it demonstrates that most of the 45 brain ROIs between AD and MCI patients have the same degree of lesion.

For the MCI/HC data set, experiments with one brain ROI removed from the ROICSE feature are also performed to find brain ROIs related to AD in classifying MCI patients from HC subjects. ACC's of the ROICSE feature with one ROI removed and the reference are shown in Fig. 10. In contrast to Fig. 9, it can be seen from Fig. 10 that still not all brain ROIs are important in MCI and HC classification, but most of the 45 brain ROIs make positive contributions to ACC, and ACC of the ROICSE approach changes from 81.71 to 83.15 percent. The first ten positive brain ROIs are 1 (precentral gyrus), 6 (inferior frontal gyrus opercular), 10 (supplementary motor area), 17 (median cingulate paracingulate gyri), 19 (hippocampus), 22 (calcarine fissure surrounding cortex), 23 (cuneus), 32 (supramarginal gyrus), 35 (paracentral lobule), and 43 (middle temporal gyrus), respectively. However, only 29 (postcentral gyrus) and 31 (inferior parietal gyri) contributes to ACC negatively and 12 (superior frontal medial) does no-contributions to ACC. As it describes, MCI, the prodromal stage of AD, has caused lesions of multiple brain regions which make a large difference between sMRI images of MCI and HC subjects. Whereas, contours of brain ROIs between MCI and HC subjects have small

changes, but detail information contained in the ROIs is largely different, so ACC of the ROICSE approach is very little affected by those negative brain ROIs.

For the MCIC/MCInc data set, experiments with one brain ROI removed from the ROICSE feature are also performed to find brain ROIs related to AD in classifying MCIC and MCInc patients, and ACC's of the ROICSE feature with one ROI removed and the reference are shown in Fig. 11. It is observed from Fig. 11 that again not all brain ROIs are important in MCIC and MCInc classification, the 45 brain ROIs are relatively and evenly classified into the positive-contribution and the negative-contribution classes, and the ACC interval of the ROICSE feature based approach is 76.03–78.76 percent. Clearly, the first ten positive brain ROIs are 6 (inferior frontal gyrus opercular), 9 (rolandic operculum), 10 (supplementary motor area), 13 (superior frontal gyrus medial orbital), 19 (hippocampus), 29 (postcentral gyrus), 30 (superior parietal gyrus), 36 (caudate nucleus), 37 (lenticular nucleus putamen), and 39 (thalamus), respectively. For the negative-contribution brain ROIs, 2 (superior frontal gyrus), 15 (insula), and 42 (temporal pole superior temporal) are remarkably significant to improve ACC, in other words, these three brain ROIs are almost no difference between sMRI images of MCIC and MCInc subjects.

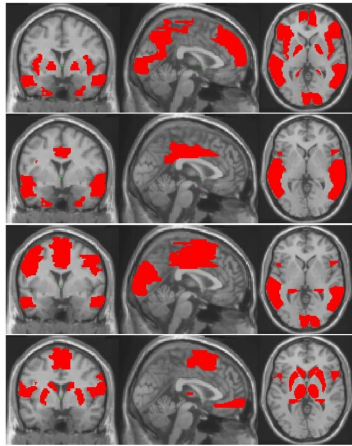


Fig. 12. First ten positive brain ROIs in classifying subjects with AD, MCI and HC on four data sets. The first row is on AD/HC data set, the second row is on AD/MCI data set, the third row is on MCI/HC data set, and the last row is on MCIc/MCInc data set.

According to the four leave-one-ROI-out experiments, we can find that different brain ROIs play different roles in classifying subjects with AD, MCI, and HC [58]. For some brain regions such as 6 (inferior frontal gyrus opercular), 28 (fusiform gyrus), and 29 (postcentral gyrus), they make positive contributions to ACC in AD classification. However, other brain regions, such as 19 (hippocampus) and 43 (middle temporal gyrus), make positive contributions to ACC in AD and MCI classification, in contrast, they make negative contributions to ACC in MCIc and MCInc classification [59]. Therefore, the selection to brain ROIs must be done before extracting energy features from their directional subbands, so that a more powerful imaging marker can be constructed to identify subjects with AD, MCI, and HC. For clarity and visualization, Fig. 12 illustrates the coronal, sagittal and axial views of the first ten positive-contribution brain ROIs that are important tissues related to AD in classification.

5 CONCLUSION

In this study, we propose an approach to perform AD classification by extracting the regions of interest (ROI)-based contourlet subband energy (ROICSE) feature. Specifically, the sMRI image, after preprocessing, is first divided into 90 different ROIs by a constructed brain mask. Instead of extracting features from the brain ROIs in the spatial domain, the contourlet transform is performed on these ROIs to obtain their subbands, and then subband energy feature vectors of different brain ROIs are concatenated to form the ROICSE feature for representing the sMRI image. Finally, results of SVM-based AD classification on six data sets show that the ROICSE approach outperforms six other state-of-the-art methods. However, experiments to find brain ROIs related to AD indicate that not all brain ROIs are important for classifying subjects with AD, MCI, and HC. Thus, feature selection is needed to construct a powerful imaging marker. In our future work, we will model associations between different brain regions in frequency domain so that those brain ROIs mostly related to AD can be selected for AD classification.

ACKNOWLEDGMENTS

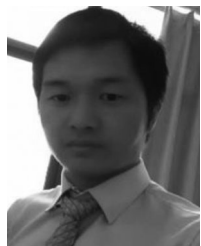
This work was supported by the National Natural Science Foundation of China (Grant No. 61873202, 61473232, 91430111, 31771476, 81471047, 31930022, 12026608 and 11871456), National Key R&D Program (Grant No. 2017YFA0505500 and 2016YFC0903400), Strategic Priority Research Program of the Chinese Academy of Sciences (Grant No. XDB38040400), and Shanghai Municipal Science and Technology Major Project (Grant No. 2017SHZDZX01). Data collection and sharing for this project was funded by the Alzheimer's Disease Neuroimaging Initiative (ADNI) (National Institutes of Health Grant U01 AG024904) and DOD ADNI (Department of Defense award number W81XWH-12-2-0012). ADNI is funded by the National Institute on Aging, the National Institute of Biomedical Imaging and Bioengineering, and through generous contributions from the following: AbbVie, Alzheimer's Association; Alzheimer's Drug Discovery Foundation; Araclon Biotech; BioClinica, Inc.; Biogen; Bristol-Myers Squibb Company; CereSpir, Inc.; Cogstate; Eisai Inc.; Elan Pharmaceuticals, Inc.; Eli Lilly and Company; EuroImmun; F. Hoffmann-La Roche Ltd and its affiliated company Genentech, Inc.; Fujirebio; GE Healthcare; IXICO Ltd.; Janssen Alzheimer Immunotherapy Research & Development, LLC.; Johnson & Johnson Pharmaceutical Research & Development LLC.; Lumosity; Lundbeck; Merck & Co., Inc.; Meso Scale Diagnostics, LLC.; NeuroRx Research; Neurotrack Technologies; Novartis Pharmaceuticals Corporation; Pfizer Inc.; Piramal Imaging; Servier; Takeda Pharmaceutical Company; and Transition Therapeutics. The Canadian Institutes of Health Research is providing funds to support ADNI clinical sites in Canada. Private sector contributions are facilitated by the Foundation for the National Institutes of Health (www.fnih.org). The grantee organization is the Northern California Institute for Research and Education, and the study is coordinated by the Alzheimer's Therapeutic Research Institute at the University of Southern California. ADNI data are disseminated by the Laboratory for Neuro Imaging at the University of Southern California.

REFERENCES

- [1] C. Lian, M. Liu, J. Zhang, and D. Shen, "Hierarchical fully convolutional network for joint atrophy localization and Alzheimer's disease diagnosis using structural MRI," *IEEE Trans. Pattern Anal. Mach. Intell.*, vol. 42, no. 4, pp. 880–893, Apr. 2020.
- [2] G. Fung and J. Stoeckel, "SVM feature selection for classification of SPECT images of Alzheimer's disease using spatial information," *Knowl. Inf. Syst.*, vol. 11, no. 2, pp. 243–258, 2007.
- [3] I. A. Illán et al., "Projecting independent components of SPECT images for computer aided diagnosis of Alzheimer's disease," *Pattern Recognit. Lett.*, vol. 31, no. 11, pp. 1342–1347, 2010.
- [4] C. Misra, Y. Fan, and C. Davatzikos, "Baseline and longitudinal patterns of brain atrophy in MCI patients, and their use in prediction of short-term conversion to AD: Results from ADNI," *NeuroImage*, vol. 44, no. 4, pp. 1415–1422, 2009.
- [5] J. Feng, S.-W. Zhang, and L. Chen, "Identification of Alzheimer's disease based on wavelet transformation energy feature of the structural MRI image and NN classifier," *Artif. Intell. Med.*, vol. 108, p. 101940, 2020.
- [6] K. Simonyan and A. Zisserman, "Very deep convolutional networks for large scale image recognition," in *Proc. Int. Conf. Learn. Representations*, 2015.

- [7] P. Cao *et al.*, "Nonlinearity-aware based dimensionality reduction and over-sampling for AD/MCI classification from MRI measures," *Comput. Biol. Med.*, vol. 91, pp. 21–37, 2017.
- [8] J. Dukart *et al.*, "Generative FDG-PET and MRI model of aging and disease progression in Alzheimer's disease," *PLoS Comput. Biol.*, vol. 9, no. 4, pp. e1002987–e1002997, 2013.
- [9] S. Liu, S. Liu, W. Cai, S. Pujol, R. Kikinis, and D. Feng, "Early diagnosis of Alzheimer's disease with deep learning," in *Proc. IEEE 11th Int. Symp. Biomed. Imag.*, 2014, pp. 1015–1018.
- [10] M. C. Carrillo *et al.*, "Worldwide Alzheimer's disease neuroimaging initiative," *Alzheimer's Dementia*, vol. 8, no. 4, pp. 337–342, 2012.
- [11] J. Zhang *et al.*, "3D texture analysis on MRI images of Alzheimer's disease," *Brain Imag. Behav.*, vol. 6, no. 1, pp. 61–69, 2012.
- [12] R. Casanova *et al.*, "High dimensional classification of structural MRI Alzheimer's disease data based on large scale regularization," *Front. Neuroinform.*, vol. 5, pp. 22–30, 2011.
- [13] J. Feng *et al.*, "Alzheimer's disease classification using features extracted from nonsubsampling contourlet subband-based individual networks," *Neurocomputing*, vol. 421, pp. 260–273, 2021.
- [14] P. Padilla, M. López, J. M. Górriz, J. Ramirez, D. Salas-Gonzalez, and I. Alvarez, "NMF-SVM based CAD tool applied to functional brain images for the diagnosis of Alzheimer's disease," *IEEE Trans. Med. Imag.*, vol. 31, no. 2, pp. 207–216, Feb. 2012.
- [15] B. Lei, P. Yang, T. Wang, S. Chen, and D. Ni, "Relational-regularized discriminative sparse learning for Alzheimer's disease diagnosis," *IEEE Trans. Cybern.*, vol. 47, no. 4, pp. 1102–1113, Apr. 2017.
- [16] Y. Cho *et al.*, "Individual subject classification for Alzheimer's disease based on incremental learning using a spatial frequency representation of cortical thickness data," *NeuroImage*, vol. 59, no. 3, pp. 2217–230, 2012.
- [17] D. Zhang *et al.*, "Multimodal classification of Alzheimer's disease and mild cognitive impairment," *NeuroImage*, vol. 55, no. 3, pp. 856–867, 2011.
- [18] S. Liu *et al.*, "Multimodal neuroimaging feature learning for multi-class diagnosis of Alzheimer's disease," *IEEE Trans. Biomed. Eng.*, vol. 62, no. 4, pp. 1132–1140, Apr. 2015.
- [19] X. Wu *et al.*, "The receiver operational characteristic for binary classification with multiple indices and its application to the neuroimaging study of Alzheimer's disease," *IEEE/ACM Trans. Comput. Biol. Bioinf.*, vol. 10, no. 1, pp. 173–180, Jan./Feb. 2013.
- [20] K. R. Gray *et al.*, "Random forest-based similarity measures for multi-modal classification of Alzheimer's disease," *NeuroImage*, vol. 65, pp. 167–175, 2013.
- [21] Y. Li *et al.*, "Discriminant analysis of longitudinal cortical thickness changes in Alzheimer's disease using dynamic and network features," *Neurobiol. Aging*, vol. 33, no. 2, pp. 427.e15–427.e30, 2012.
- [22] Y. He, Z. Chen, and A. Evans, "Structural insights into aberrant topological patterns of large-scale cortical networks in Alzheimer's disease," *J. Neurosci.*, vol. 28, no. 18, pp. 4756–4766, 2008.
- [23] D. Dai *et al.*, "Accurate prediction of AD patients using cortical thickness networks," *Mach. Vis. Appl.*, vol. 24, no. 7, pp. 1445–1457, 2013.
- [24] G. Chen *et al.*, "Classification of Alzheimer disease, mild cognitive impairment, and normal cognitive status with large-scale network analysis based on resting-state functional MR imaging," *Radiology*, vol. 259, no. 1, pp. 213–221, 2011.
- [25] C. Y. Wee *et al.*, "Resting-state multi-spectrum functional connectivity networks for identification of MCI patients," *PLoS One*, vol. 7, no. 5, pp. e37828–e37838, 2012.
- [26] L. Cao *et al.*, "Multi-task neural networks for joint hippocampus segmentation and clinical score regression," *Multimedia Tools Appl.*, vol. 77, pp. 29669–29686, 2018.
- [27] M. Chupin *et al.*, "Fully automatic hippocampus segmentation and classification in Alzheimer's disease and mild cognitive impairment applied on data from ADNI," *Hippocampus*, vol. 19, no. 6, pp. 579–587, 2009.
- [28] K. R. Gray *et al.*, "Multi-region analysis of longitudinal FDG-PET for the classification of Alzheimer's disease," *NeuroImage*, vol. 60, no. 1, pp. 221–229, 2012.
- [29] N. Schuff *et al.*, "MRI of hippocampal volume loss in early Alzheimer's disease in relation to ApoE genotype and biomarkers," *Brain*, vol. 132, no. 4, pp. 1067–1077, 2009.
- [30] B. Magnin, L. Mesrob, and S. Kinkingnéhun, "Support vector machine-based classification of Alzheimer's disease from whole-brain anatomical MRI," *Neuroradiology*, vol. 51, no. 2, pp. 73–83, 2009.
- [31] J. Liu, M. Li, W. Lan, F.-X. Wu, Y. Pan, and J. Wang, "Classification of Alzheimer's disease using whole brain hierarchical network," *IEEE/ACM Trans. Comput. Biol. Bioinf.*, vol. 55, no. 2, pp. 624–632, Mar./Apr. 2018.
- [32] L. Clerx, I. A. V. Rossum, and L. Burns, "Measurements of medial temporal lobe atrophy for prediction of Alzheimer's disease in subjects with mild cognitive impairment," *Neurobiol. Aging*, vol. 34, no. 8, pp. 2003–2013, 2013.
- [33] R. Ju, C. Hu, P. Zhou, and Q. Li, "Early diagnosis of Alzheimer's disease based on resting-state brain networks and deep learning," *IEEE/ACM Trans. Comput. Biol. Bioinf.*, vol. 16, no. 1, pp. 244–257, Jan./Feb. 2019.
- [34] Y. Fan *et al.*, "Spatial patterns of brain atrophy in MCI patients, identified via high-dimensional pattern classification, predict subsequent cognitive decline," *NeuroImage*, vol. 39, no. 4, pp. 1731–1743, 2008.
- [35] M. López, J. Ramírez, and J. M. Górriz, "Principal component analysis-based techniques and supervised classification schemes for the early detection of Alzheimer's disease," *Neurocomputing*, vol. 74, no. 8, pp. 1260–1271, 2011.
- [36] D. Salas-Gonzalez, D. Górriz, and J. Ramírez, "Feature selection using factor analysis for Alzheimer's diagnosis using PET images," *Med. Phys.*, vol. 37, no. 11, pp. 6084–6095, 2010.
- [37] O. B. Ahmed *et al.*, "Classification of Alzheimer's disease subjects from MRI using hippocampal visual features," *Multimedia Tools Appl.*, vol. 74, no. 4, pp. 1249–1266, 2015.
- [38] H. Li *et al.*, "A deep learning model for early prediction of Alzheimer's disease dementia based on hippocampal magnetic resonance imaging data," *Alzheimer's Dementia*, vol. 15, no. 8, pp. 1059–1070, 2019.
- [39] L. Khedher, J. Ramírez, and J. M. Górriz, "Early diagnosis of Alzheimer's disease based on partial least squares, principal component analysis and support vector machine using segmented MRI images," *Neurocomputing*, vol. 151, pp. 139–150, 2015.
- [40] J. Feng *et al.*, "Structural difference histogram representation for texture image classification," *IET Image Process.*, vol. 11, no. 2, pp. 118–125, 2016.
- [41] D. Jha and G. R. Kwon, "Contourlet-based feature extraction for computer-aided classification of Alzheimer's disease," *Alzheimer's Dis.: J. Alzheimer's Assoc.*, vol. 14, no. 7, 2018.
- [42] N. Gao *et al.*, "Contourlet-based hippocampal magnetic resonance imaging texture features for multivariate classification and prediction of Alzheimer's disease," *Metabolic Brain Dis.*, vol. 33, no. 6, pp. 1899–1909, 2018.
- [43] J. Wen *et al.*, "Convolutional neural networks for classification of Alzheimer's disease: Overview and reproducible evaluation," *Med. Image Anal.*, vol. 63, p. 101694, 2020.
- [44] M. Liu *et al.*, "A multi-model deep convolutional neural network for automatic hippocampus segmentation and classification in Alzheimer's disease," *NeuroImage*, vol. 208, 2020.
- [45] S. Wang *et al.*, "Classification of Alzheimer's disease based on eight-layer convolutional neural network with leaky rectified linear unit and max pooling," *J. Med. Syst.*, vol. 42, 2018.
- [46] Y. Dong, J. Feng, L. Liang, L. Zheng, and Q. Wu, "Multiscale sampling based texture image classification," *IEEE Signal Process. Lett.*, vol. 24, no. 5, pp. 614–618, May 2017.
- [47] Y. Zhang *et al.*, "Multivariate approach for Alzheimer's disease detection using stationary wavelet entropy and predator-prey particle swarm optimization," *J. Alzheimer's Dis.*, vol. 65, no. 3, pp. 855–869, 2018.
- [48] D. Jha *et al.*, "Alzheimer's disease detection using extreme learning machine, complex dual tree wavelet principal coefficients and linear discriminant analysis," *J. Med. Imag. Health Inform.*, vol. 8, no. 5, pp. 881–890, 2018.
- [49] N. Tzourio-Mazoyer *et al.*, "Automated anatomical labeling of activations in SPM using a macroscopic anatomical parcellation of the MNI MRI single-subject brain," *NeuroImage*, vol. 15, no. 1, pp. 273–289, 2002.
- [50] J. Ashburner *et al.*, "Statistical parametric Mapping," *Practical Neurology*, vol. 4, no. 6, pp. 350–355, 2004.
- [51] J. Ashburner and K. J. Friston, "Voxel-based morphometry-the methods," *NeuroImage*, vol. 11, no. 6, pp. 805–821, 2000.
- [52] M. N. Do and M. Vetterli, "The contourlet transform: An efficient directional multiresolution image representation," *IEEE Trans. Image Process.*, vol. 14, no. 12, pp. 2091–2106, Dec. 2005.
- [53] M. W. Wener *et al.*, "The Alzheimer's disease neuroimaging initiative: A review of papers published since its inception," *Alzheimer's Dementia*, vol. 9, no. 5, pp. e111–e194, Apr. 2013.
- [54] J. G. Sled, A. P. Zijdenbos, and A. C. Evans, "A nonparametric method for automatic correction of intensity nonuniformity in MRI data," *IEEE Trans. Med. Imag.*, vol. 17, no. 1, pp. 87–97, Feb. 1998.

- [55] R. Cuingnet *et al.*, "Automatic classification of patients with Alzheimer's disease from structural MRI: A comparison of ten methods using the ADNI database," *NeuroImage*, vol. 56, no. 2, pp. 766–781, 2011.
- [56] D. Pachauri, C. Hinrichs, M. K. Chung, S. C. Johnson, and V. Singh, "Topology-based kernels with application to inference problems in Alzheimer's disease," *IEEE Trans. Med. Imag.*, vol. 30, no. 10, pp. 1760–1770, Oct. 2011.
- [57] X. Yang, M. Z. Tan, and A. Qiu, "CSF and brain structural imaging markers of the Alzheimer's pathological cascade," *PLoS One*, vol. 7, no. 12, pp. e47406–e47412, 2012.
- [58] Q. Zhou *et al.*, "An optimal decisional space for the classification of Alzheimer's disease and mild cognitive impairment," *IEEE Trans. Biomed. Eng.*, vol. 61, no. 8, pp. 2245–2253, Aug. 2014.
- [59] R. C. Petersen, "Mild cognitive impairment as a diagnostic entity," *J. Internal Med.*, vol. 256, no. 3, pp. 183–194, 2004.
- [60] T. Ye *et al.*, "Discriminative multi-task feature selection for multimodality classification of Alzheimer's disease," *Brain Imag. Behav.*, vol. 10, no. 3, pp. 739–749, 2016.
- [61] J. Zhang, Y. Gao, Y. Gao, B. C. Munsell, and D. Shen, "Detecting anatomical landmarks for fast Alzheimer's disease diagnosis," *IEEE Trans. Med. Imag.*, vol. 35, no. 12, pp. 2524–2533, Dec. 2016.
- [62] D. R. Nayak, R. Dash, X. Chang, B. Majhi, and S. Bakshi, "Automated diagnosis of pathological brain using fast curvelet entropy features," *IEEE Tans. Sustain. Comput.*, vol. 5, no. 3, pp. 416–427, Third Quarter 2020.
- [63] Y. Dong and J. Ma, "Feature extraction through contourlet subband clustering for texture classification," *Neurocomputing*, vol. 116, pp. 157–164, 2013.



Jinwang Feng received the BS degree from the Luoyang Institute of Science and Technology, Luoyang, China, in 2010, and the MS degree from the Henan University of Science and Technology, Luoyang, China, in 2017. He is currently working toward the PhD degree at Northwestern Polytechnical University, Xi'an, China, since 2018. He was a teacher with Zhengzhou Technical College between 2017 and 2018. Now, he is studying with the Key Laboratory of Systems Biology, Shanghai Institute of Biochemistry and Cell

Biology, Center for Excellence in Molecular Cell Science, Chinese Academy of Sciences. His current research interests include medical image processing, pattern recognition, machine learning, and computer vision.



Shao-Wu Zhang received the PhD degree in control theory and control engineering from Northwestern Polytechnical University, Xi'an, China. He is currently a professor with the School of Automation, Northwestern Polytechnical University, China. He worked as a visiting scholar with the Department of Electrical and Computer Engineering, University of Texas San Antonio, USA, in May 2016; as a visiting scholar and staff with the Computational Biology and Bioinformatics Group, University of Southern California, USA from 2008 to 2009; as a staff with the Department of Computing, Hong Kong Polytechnic University in August 2008. His recent interests include RNA methylation pattern mining, complex biological networks, brain imaging genomics, lncRNA prediction, drug-target prediction, metagenomics, applications of pattern recognition theory and machine learning to bioinformatics and biological systems.



Luonan Chen received the BS degree from the Huazhong University of Science and Technology, Wuhan, China, in 1984, and the MS and PhD degrees from Tohoku University, Sendai, Japan, in 1988 and 1991, respectively. Since 2010, he has been a professor and executive director with the Key Laboratory of Systems Biology, Shanghai Institutes for Biological Sciences, Chinese Academy of Sciences. His fields of interests are computational systems biology, bioinformatics, and nonlinear dynamics. In recent years, he published

more than 350 journal papers and two monographs in the area of computational systems biology.

► **For more information on this or any other computing topic, please visit our Digital Library at www.computer.org/csdl.**